

## Research Paper

# Correlations of laser scanning parameters and porous structure properties of permeable materials made by laser-beam powder-bed fusion

Dongxu Xie, Roland Dittmeyer\*

Institute for Micro Process Engineering (IMVT), Karlsruhe Institute of Technology (KIT), 76344 Eggenstein-Leopoldshafen, Germany

## ARTICLE INFO

## Keywords:

Additive manufacturing  
Additively manufactured permeable material  
Permeable-dense composite

## ABSTRACT

Laser-beam powder bed fusion (LB-PBF) of metals is an additive manufacturing (AM) method currently being pursued in numerous industries. In this study, the effect of scan strategy, laser spot size, and hatch distance on the pore structure of additively manufactured permeable stainless steel materials was systematically studied through the analysis of material permeability, pore size distribution, porosity, and surface morphology. When the hatch distance is wide and laser power is low, two kinds of pores are formed and were studied. The first one is pores located between laser-melted tracks, the second type is pores generated inside the laser-melted tracks. Scan strategy and laser spot size have no obvious effect on the porosity, but they affect the powder attached on the surface, the permeability, and the pore size of the permeable material. Hatch distance plays an important role in controlling the material properties. When the hatch distance is larger than 0.13 mm, the effect of powder attached on the surface on the pore structure of the permeable material is weakened, and the permeability increases significantly. By optimizing these parameters, permeable materials with pore sizes ranging from 2.6 to 13.7  $\mu\text{m}$  and a thickness of 0.89 mm were fabricated. To illustrate the potential of the method, for the first time an additively manufactured planar permeable-dense metallic membrane substrate with internal flow channels was fabricated, which is a center piece of a new compact modular integrated membrane reformer system.

## 1. Introduction

LB-PBF is an additive manufacturing technology that has been widely used in aerospace and automotive manufacturing [1]. By melting the metal powder layer by layer with a laser, LB-PBF can produce completely geometrically dense parts. For example, in order to avoid pores affecting the mechanical properties of the parts, Buchbinder et al. obtained 99.5% of the theoretical density of LB-PBF-generated aluminum (AlSi10Mg) by optimizing the parameters [2]. However, a defined porosity, pore size and permeability are desired in some applications, such as membrane supports, filter components [3], and artificial bones [4]. Stoffregen et al. divided additively manufactured porous materials into two categories: (i) geometrically defined lattice structure porosity (GDLSP) and (ii) geometrically undefined porosity (GUP) [5]. Porosity and pore sizes of GDLSP-type materials are determined by different lattice structures and strut thicknesses which can be designed by a CAD model [6]. In GUP-type materials, porosity and pore size are determined by laser parameters [7]. Therefore, the pore structure in the

case of GUP is random. However, the relationship between parameters and pore structure has not yet been systematically studied. Generally, the pore size range of GUP-type materials is from 1 to 100  $\mu\text{m}$ , whereas for GDLSP-type materials it is typically larger, i.e., from 100  $\mu\text{m}$  to 1 mm.

For some applications such as artificial bones, GDLSP's high porosity characteristics are more suitable [8]. However, if the pore size of a permeable material has to be smaller than 100  $\mu\text{m}$ , e.g., for being used as a membrane support, GDLSP is not applicable anymore [9]. Moreover, with proper control of the printing parameters, materials with both GUP and dense characteristics can be printed in one step by LB-PBF. Such permeable-dense composites show big potential for application in process engineering. Composite membranes may serve as one example. More specifically, Boeltken et al. reported a new method for coating of Pd membranes for  $\text{H}_2$  separation on planar porous substrates. Suspension plasma spraying (SPS) of Pd nanoparticles was used showing several advantages here with a view to industrial implementation, e.g., quick deposition [10]. However, in applications like this, the permeable membrane support is usually combined with a dense material, e.g., by

*Abbreviations:* LB-PBF, Laser-beam powder bed fusion; GDLSP, Geometrically defined lattice structure porosity; GUP, geometrically undefined porosity; SEM, Scanning electron microscopy; MOFs, Metal organic frameworks; SCR, Self-catalytic reactors.

\* Corresponding author.

E-mail address: [roland.dittmeyer@kit.edu](mailto:roland.dittmeyer@kit.edu) (R. Dittmeyer).

<https://doi.org/10.1016/j.addma.2021.102261>

Received 8 March 2021; Received in revised form 20 July 2021; Accepted 17 August 2021

Available online 1 September 2021

2214-8604/© 2021 The Authors.

Published by Elsevier B.V. This is an open access article under the CC BY-NC-ND license

(<http://creativecommons.org/licenses/by-nc-nd/4.0/>).

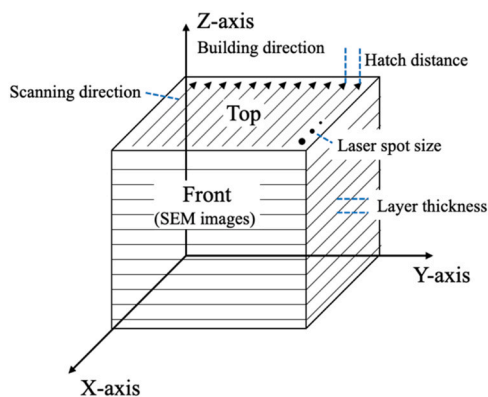


Fig. 1. Basic laser scanning parameters. Coordinates refer to the printer's coordinate system.

welding to enable reliable sealing and easy assembly. The weld seam formed turns out as a critical region for any membrane layer coated on top of the support. These regions are prone to the formation of local defects in the final palladium membrane or in the required permeable ceramic interlayer underneath as well as to low adhesion of the coating. Both degrades membrane quality [11]. Given this, a permeable-dense composite material prepared in one step by LB-PBF and with smooth transition from the permeable to the dense part would be a feasible solution [12]. To give another example, Siemens recently presented a novel rotating component made from a porous-dense composite created by LB-PBF to counter-act vibrations [13]. And also in the lab, additively manufactured porous materials attract more and more interest [14]. For example, Cheng et al. fabricated three-dimensional graphene based on an additively manufactured porous copper template [15], and Arenas et al. made additively manufactured porous electrodes for electrochemical flow reactors [16]. Stoia et al. studied the correlation between printing parameters and the mechanical properties of porous polyamide-aluminum (alumide) composite materials [17,18]. For application as a substrate for composite palladium membranes, sufficiently high permeability, low roughness and small pore size on the surface where the membrane is to be applied as well as adequate thickness to provide sufficiently high mechanical strength are necessary. Generally, GUP materials with controllable porosity are fabricated by adjusting parameters such as scan speed [19], hatch distance [20], and laser power [21] reducing the energy density. However, in this way, the permeability, roughness and thickness are in conflict with each other. Abele et al. published additively manufactured porous materials with a pore size range from 7 to 16  $\mu\text{m}$ . When the material got thicker than 200  $\mu\text{m}$ , it was no more permeable. To address this issue, in the present study the pore structure was adjusted by controlling the laser spot size, the hatch distance, and the scanning direction. The influence of different

parameters on the pore structure was studied in detail and systematically.

## 2. Materials and methods

### 2.1. System and material

316L stainless steel powder with a size of 10–45  $\mu\text{m}$  provided by LPW Technology Ltd (United Kingdom) and a Realizer SLM125 (Germany) LB-PBF machine were used in this study. 316L stainless steel is a standard material for LB-PBF and a good choice for many applications which do not involve temperatures higher than 300  $^{\circ}\text{C}$  or aggressive media. Most of the applications currently under development at the Institute for Micro Process Engineering fall into this category. Therefore, this material was also used for the study on 3D printed permeable materials in this paper.

As shown in Fig. 1, parameters including hatch distance  $s_{\text{hatch}}$ , laser spot size  $d_{\text{LS}}$ , scanning direction, etc., can be controlled in the Realizer SLM125 operating system. For all samples, the laser power was 80 W, the layer thickness 50  $\mu\text{m}$ , the scan speed 1000 mm/s (laser point distance: 40  $\mu\text{m}$ , exposure time: 40  $\mu\text{s}$ ). In the conventional approach, the laser will first scan the outer line of each layer, which is the external boundary shown in Fig. 1. In this study, in order to prepare permeable materials and to investigate the influence of different parameters on the material properties, all samples were made without external boundary scanning.

In this study, as shown in Fig. 2, the effect of different scanning strategies on the pore structure was investigated. All micrographs shown in this study were taken from the front surface of the produced samples.

As shown in Table 1, 12 samples were prepared to investigate the influence of scan strategies and laser parameters on the permeability, roughness, pore size, and porosity of the permeable materials. T-1 and T-2 samples were fabricated with different laser spot diameter in order to explore the structure of a surface composed of the side borders of the

Table 1  
Parameter set for each print condition and the corresponding print ID.

Print ID	Hatch distance/mm	Laser spot diameter/ $\mu\text{m}$	Scan strategy
T-1	0.1	50	B
T-2	0.1	30	B
T-3	0.1	50	A
T-4	0.1	50	C
T-5	0.1	30	A
T-6	0.1	40	A
T-7	0.1	60	A
T-8	0.11	50	A
T-9	0.12	50	A
T-10	0.13	50	A
T-11	0.14	50	A
T-12	0.15	50	A

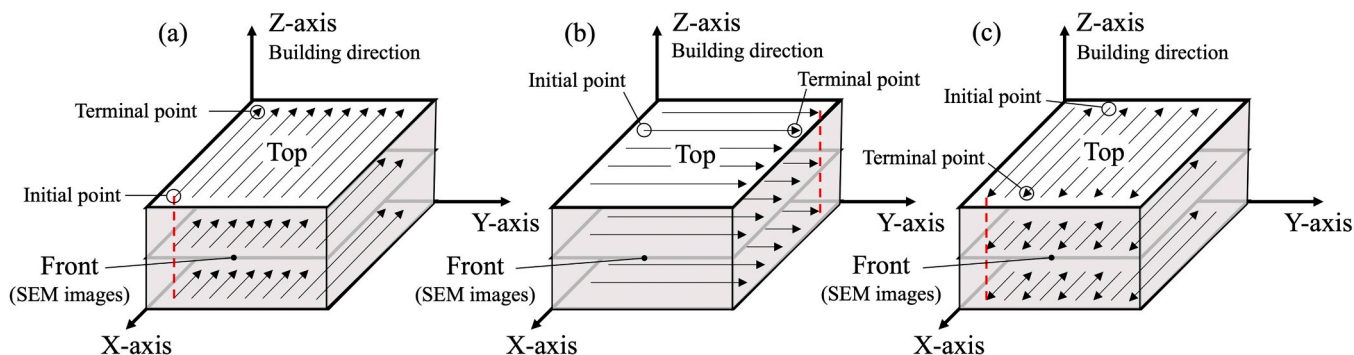


Fig. 2. (a) Scan strategy A: X direction with unidirectional scan vectors; (b) Scan strategy B: Y direction with unidirectional scan vectors; (c) Scan strategy C: unidirectional scan vectors arranged alternately opposite in X direction. Coordinates refer to the printer's coordinate system.

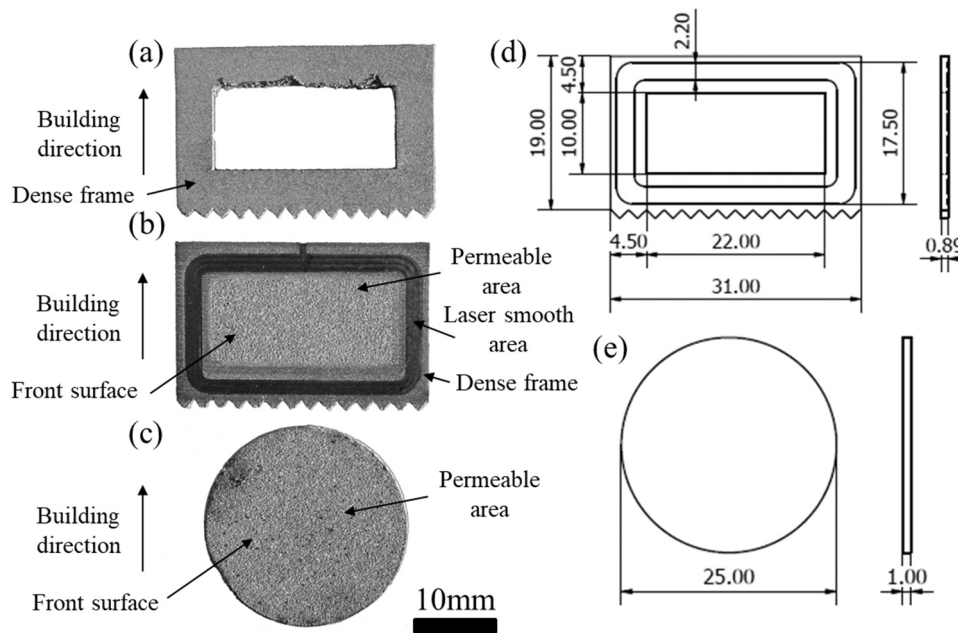


Fig. 3. (a) Dense frame for porosity measurements (b) Permeable-dense composite sample for permeability and porosity measurements (c) Disk-shaped permeable sample for pore size distribution measurements.

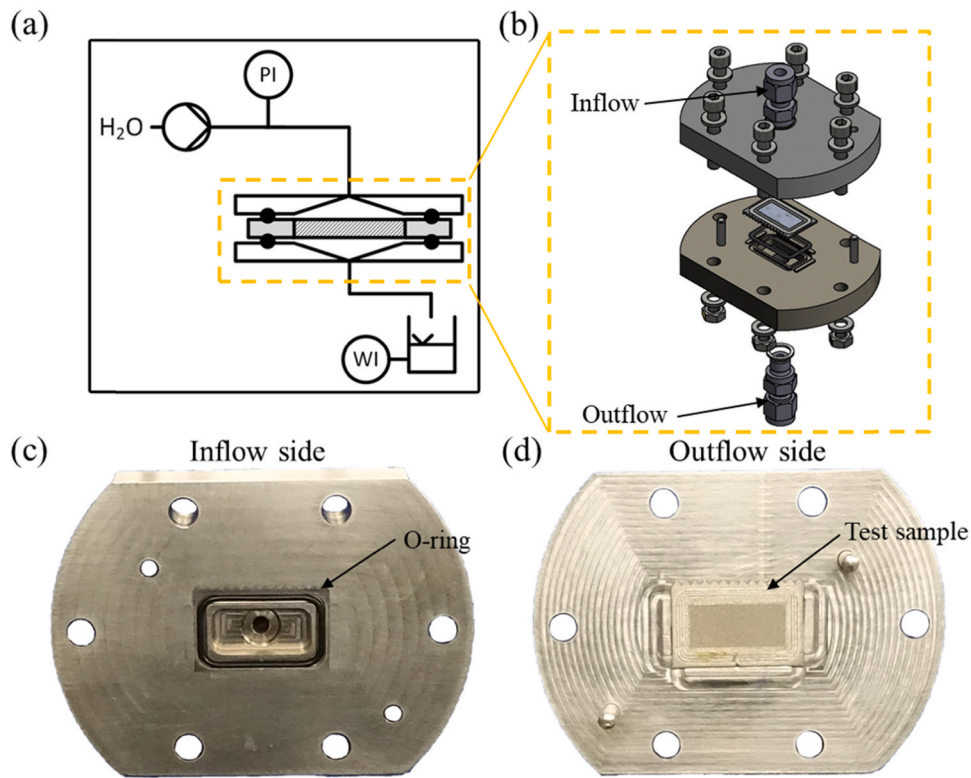


Fig. 4. Flow cell system for permeability measurements.

scan vectors. Samples T-3 to T-12 were used to investigate the porous structures fabricated with different hatch distance and laser spot size by scan strategies A and C. In order to avoid the influence of other

unforeseen factors, all samples were printed in the same batch. Note that scan strategies A and B only differ in the orientation of the unidirectional scan vectors relative to the printer's coordinate system but basically

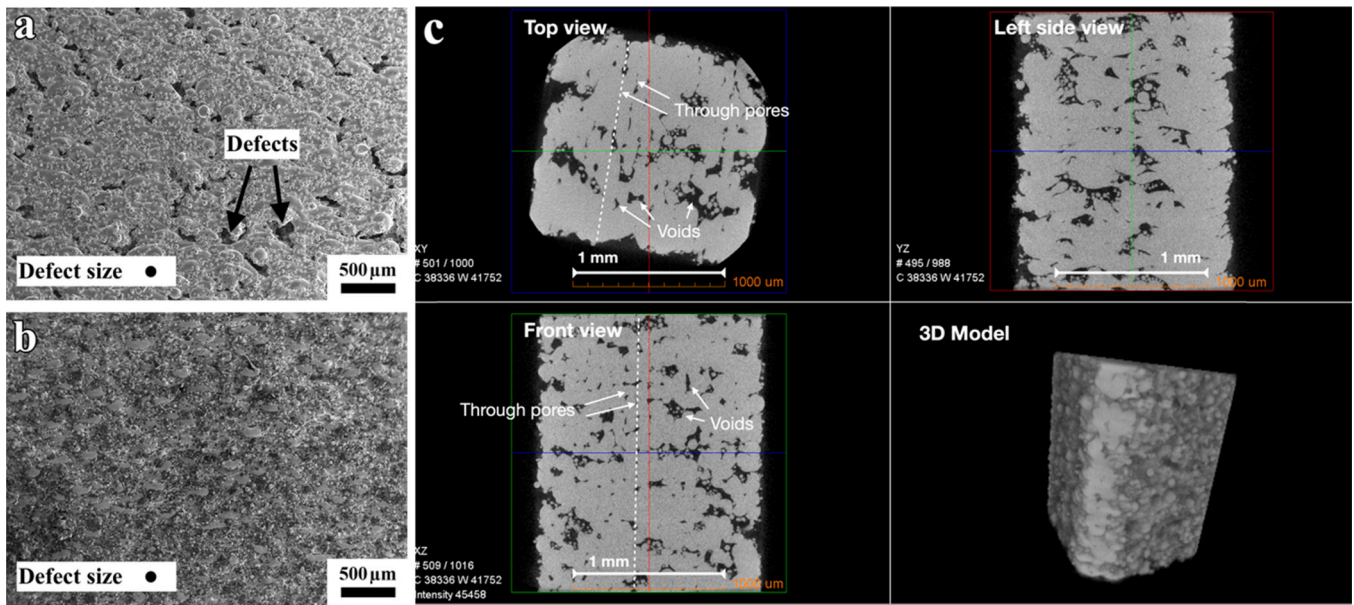


Fig. 5. (a) SEM micrograph (magnification:  $\times 25$ ) of the front surface of a sample produced by scan strategy B with 50  $\mu\text{m}$  laser spot diameter (T-1); (b) SEM micrograph (magnification:  $\times 25$ ) of the front surface of a sample produced by scan strategy B with 30  $\mu\text{m}$  laser spot diameter (T-2); (c)  $\mu\text{-CT}$  scan model of a sample printed with unidirectional scan vectors according to scan strategy A with 50  $\mu\text{m}$  laser spot diameter (T-3). Note that the front of sample T-1 shown in (a) is the same face as the left (or right) side of sample T-3 shown in (c).

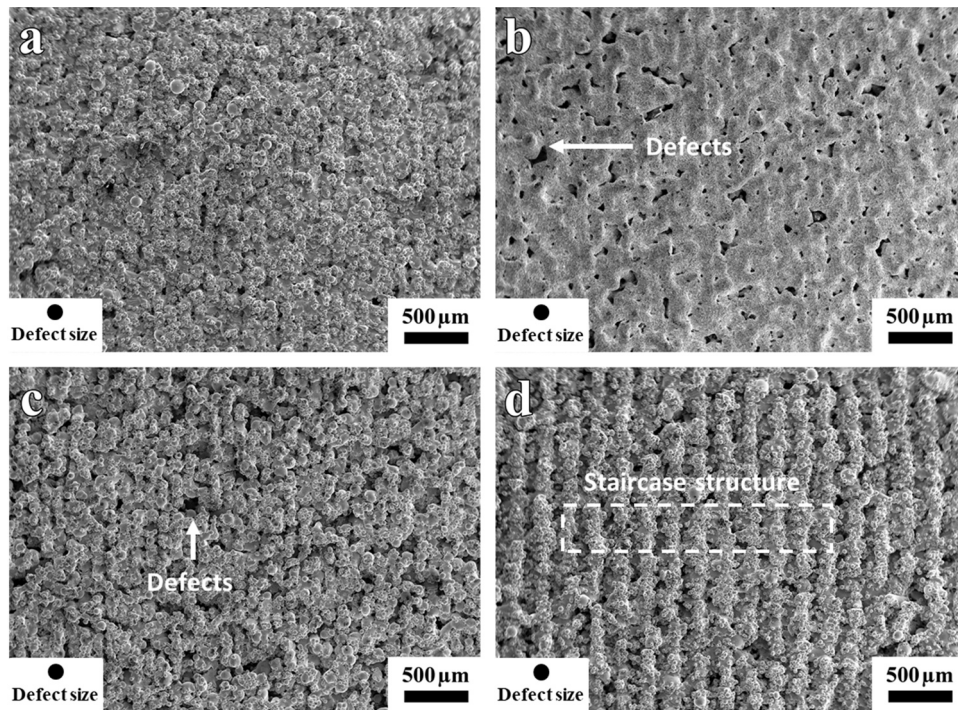


Fig. 6. (a) SEM micrograph (magnification:  $\times 25$ ) of the front surface of the sample produced by scan strategy A (T-3); (b) SEM micrograph (magnification:  $\times 25$ ) of the front surface of sample T-3 after sand blasting treatment; (c) SEM micrograph (magnification:  $\times 25$ ) of the back surface of sample T-3. (d) SEM micrograph (magnification:  $\times 25$ ) of the front surface of the sample produced by scan strategy C (T-4).

produce the same type of sample.

For determination of the porosity and for permeation tests (see Sections 2.2 and 2.4), permeable-dense composite test samples with a

dense frame surrounding the permeable part were printed. For measurement of the pore size distribution, disk-shaped completely permeable test samples were used. Exemplary photographs and dimensions are

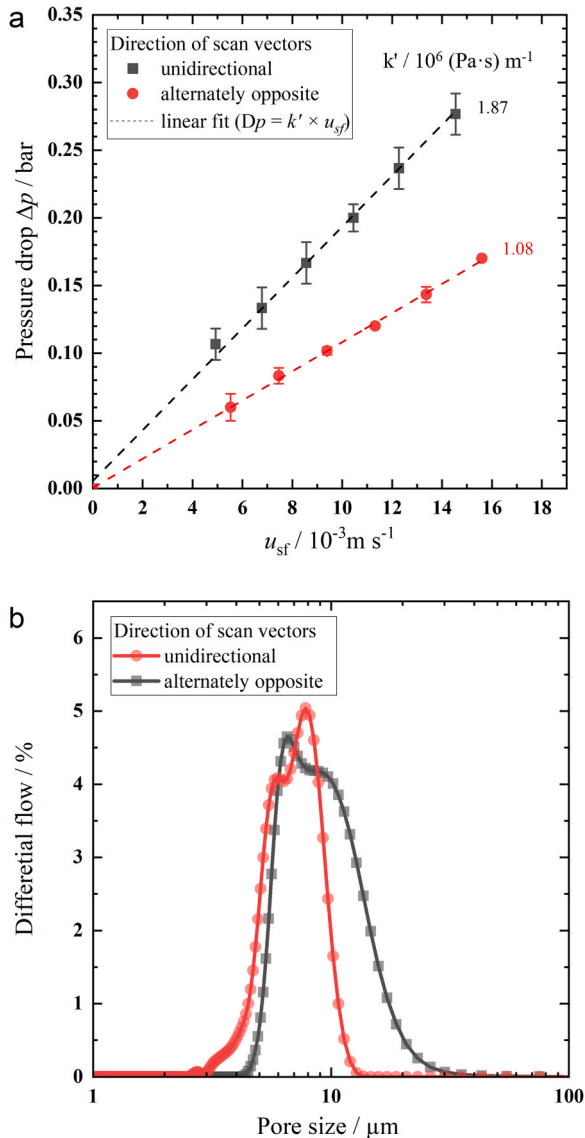


Fig. 7. (a) Permeation testing of samples with different scanning direction; (b) Pore size distribution of samples with different scanning direction.

shown in Fig. 3.

## 2.2. Determination of porosity and pore size distribution

The porosity was calculated following Eq. (1).

$$\varepsilon = \left(1 - \frac{m_{s,\text{por}} \cdot \rho_{\text{met}}^{-1}}{A_{\text{por}} \cdot s_{s,\text{por}}}\right) \times 100\% \quad (1a)$$

with

$$m_{s,\text{por}} = m_{s,\text{tot}} - m_{s,\text{den}} \quad (1b)$$

Where  $m_{s,\text{por}}$  is the mass of the permeable part only, as calculated by Eq. (1b) with  $m_{s,\text{tot}}$  being the total mass measured for each individual test sample (via precision balance,  $\pm 1$  mg) and  $m_{s,\text{den}} = 2.565$ g is the mass of the dense part only, determined from a frame test sample printed without the permeable part. The dense part of the test samples was smoothed by laser treatment (*TruCell 3010 Trumpf*) for better sealing. In order to avoid the influence of laser smoothing on weight, all test samples were weighed before laser smoothing. The thickness of the permeable part  $s_{s,\text{por}} = 890$ μm was measured via a 3D optical

Table 2

Roughness, porosity and permeability of samples with different scanning direction.

Print ID	T-3	T-4
Scan strategy	A	C
Roughness (μm)	20.37 ± 0.72	30.88 ± 0.73
Porosity	17%	18%
Permeability (m <sup>2</sup> )	4.81 ± 0.14E-13	8.32 ± 0.16E-13

profilometer (*Sensofar S-neox*, resolution: 0.31 μm). Its area  $A_{s,\text{por}}$  was defined by the dimensions given in the CAD model ( $l_{\text{por},y} \times l_{\text{por},z}$ : 22 mm × 10 mm) and measured by a caliper to ensure the error is less than 0.1 mm. The density  $\rho_{\text{met}}$  is the bulk density of the metal (316L stainless steel, 8 g cm<sup>-3</sup> [22]).

The pore size distribution of the permeable samples was measured by capillary flow porometry with a *Porometer 3G*. Disk-shaped samples of 25 mm diameter and 1 mm thickness fabricated with different parameters were investigated. In this method, the sample is first immersed in a dedicated measuring liquid characterized by good wetting ability, low surface tension, and low vapor pressure (i.e. *POROFIL Quantachrome* for the 316L samples investigated in this study) for 10 min to fill all pores of the sample completely. Then the sample is placed in the porometer, and the air is gradually pressurized to displace the liquid from the pores starting from the largest to the smallest pores present in the sample. This results in a gas pressure vs. flow curve (wet curve). Subsequently, the gas pressure is gradually decreased to determine the corresponding gas pressure vs. flow curve of the dry sample (dry curve). Per sample 256 data points of pressure  $\Delta p_n$  and corresponding gas flow  $\dot{V}_n$  were acquired for both, wet and dry curve. According to the Washburn formula, different pressures correspond to different pore sizes as shown in Eq. (2) [23]:

$$\Delta p \cdot r_{\text{pore}} = 2\gamma_f \cos\theta_f \quad (2)$$

Where  $\Delta p$  is the pressure difference over the sample,  $r_{\text{pore}}$  is the radius of the pore,  $\gamma_f$  is surface tension of the fluid,  $\theta_f$  is the contact angle between the fluid and the solid surface (for gases penetrating a pore ( $\theta_f = 0^\circ$ ), Eq. (2) reduces to  $\Delta p \cdot r_{\text{pore}} = 2\gamma_f$ ). From the measured data  $\dot{V}_{n,\text{wet}}(\Delta p_n)$  resp.  $\dot{V}_{n,\text{dry}}(\Delta p_n)$  for the 256 data points, a flow-based pore size distribution  $v_{\text{diff}}(r_{\text{pore}} = f(\Delta p))$  can be deduced from the cumulative flow values at distinct ( $n$ ) pressure values according to Eqs. (2)–(4) [24].

$$v_{\text{cum},n} = \frac{\dot{V}_{n,\text{wet}}(\Delta p_n)}{\dot{V}_{n,\text{dry}}(\Delta p_n)}; n = 1 \dots 256 \quad (3)$$

$$v_{\text{diff},n} = \frac{(v_{\text{cum}})_{n+1} - (v_{\text{cum}})_{n-1}}{2}; n = 1 \dots 255 \quad (4)$$

Note that  $n$  refers to a distinct pressure difference at which all pores of the size defined by Eq. (2) or larger will be opened for the gas flow when starting from a liquid-filled state. Note also that this method always detects the narrowest cross-section of a through-pore and reflects a flow-based pore size distribution rather than a volume or number-based pore size distribution.

## 2.3. Determination of permeability

The permeability was tested using a flow cell system by measuring the pressure loss at variable flow rates of water permeating through the test sample (see Fig. 4). The dense part was first smoothed by laser treatment (see Fig. 3), then sealing via the dense part of the tested sample was achieved using polymer O-rings. The pressure was measured using a *Baumer PBSN* pressure sensor (range from 0 to 2.5 bar absolute, standard error of measurement  $\pm 0.03\%$  FSP). The water flow rate was controlled by a *Verdergear VG 1000* basic gear pump. The flow rate was varied from 30% to 80% of the maximum rating of 4000 rpm with 10%

interval and precisely determined for each setting by measuring the amount of water (balance) permeating over 2 min. At the beginning of each permeation test, the flow cell system was run for 30 min to guarantee stable conditions (sample completely wetted, constant flow rate and pressure loss). During the measurement procedure, the system was allowed to equilibrate for at least 5 min after setting a higher flux before measuring the corresponding pressure loss. Based on the amount of water permeating within 120 s, the superficial velocity was calculated based on Eq. (5) with  $\rho_{\text{H}_2\text{O}} = 998 \text{ kg}\cdot\text{m}^{-3}$  and  $A_{\text{s,por}} = 2.2 \text{ cm}^2$  (see also Section 2.2).

$$u_{\text{sf}} = \frac{m_{\text{H}_2\text{O}}}{\Delta t} \cdot \rho_{\text{H}_2\text{O}}^{-1} \cdot A_{\text{s,por}}^{-1} \quad (5)$$

A linear dependency of the pressure drop on the superficial velocity of a fluid permeating a porous medium can be described by Darcy's law:

$$\Delta p = u_{\text{sf}} \cdot \frac{\mu \cdot s}{K} \quad (6)$$

Where  $K$  is the permeability of the porous medium (in  $\text{m}^2$ ),  $\Delta p$  is the pressure loss from inlet to outlet (in Pa, absolute numbers),  $\mu$  is the dynamic viscosity of the fluid (here: water 20 °C, 1.01 mPa s) and  $s$  is the thickness of the porous medium (here:  $s$  equals the thickness of the permeable part  $s_{\text{s,por}} = 890 \text{ }\mu\text{m}$ ).

## 2.4. Sand blasting

Sand blasting was used to remove the powder sintered on the samples' surface to see the pore structure below. The system pressure during sand blasting was 2.5 bar, and a F150 corundum grit was used.

## 2.5. Morphology

The surface roughness (arithmetic mean height of the surface:  $S_a$ ) was investigated by a 3D optical profiler (*S-neox, Sensofar* with ISO 25178), and the surface morphology was studied by scanning electron microscopy (SEM, *JSM 6300, Jeol* with a 10 kV beam). 3D structure characterization was done by  $\mu$ -CT measurements (*ZEISS, Xradia 520 Versa*) at the Institute of Mechanical Process Engineering and Mechanics (MVM) of the Karlsruhe Institute of Technology (KIT).

## 2.6. Ceramic coating

In order to avoid the diffusion of metal atoms from the 316L stainless steel substrate into the palladium membrane, a diffusion barrier layer (DBL) made of Yttria Stabilized Zirconia (8YSZ) between the metallic substrate and the palladium membrane was fabricated [9]. The coating was carried out at the Institute for Energy and Climate Research 1 (IEK-1) of the Research Center Jülich (FZJ).

# 3. Results and discussion

## 3.1. Pore structures in different scan strategy

### 3.1.1. Scanning direction parallel to the front surface

Fig. 5 shows the micrographs of samples T-1 and T-2. The scan strategy of T-1 and T-2 was scan strategy B: Y direction with unidirectional scan vectors. The varied parameter for the two samples is the laser spot size. The laser spot size of T-1 was 50  $\mu\text{m}$  and that of T-2 was 30  $\mu\text{m}$ .

To make it easier for discussion, as shown in Fig. 2, all micrographs were taken from the front surface. Although the laser power of two samples was the same, the surfaces of the two samples are different. Since the aim of this work is to produce permeable materials with pore sizes well below 100  $\mu\text{m}$ , pores larger than 100  $\mu\text{m}$  are defined as defects. T-1 in Fig. 5(a) shows a surface with lots of defects while T-2 in Fig. 5(b) shows a surface without pores. As can be seen in Fig. 2, the front surface of scan strategy B are defects caused by not fully melted powder in single tracks. Therefore, the pore size and pore distribution of the permeable material according to strategy B are quite random. Note that the laser power of T-2 was the same as for T-1. Better single track quality with smaller laser spot size apparently caused the pores to disappear.

To provide an exemplary 3-dimensional picture of the pore structure, Fig. 5(c) shows the  $\mu$ -CT scan results of the sample T-3 printed with unidirectional scan vectors according to scan strategy A with 50  $\mu\text{m}$  laser spot diameter. The through-pores visible in outlines in the top and front views have a small pore size and a direction parallel to the laser tracks. The porosity is mainly contributed by voids in the material which are randomly distributed along these through pores. The cross-sectional images indicate that parts of the laser tracks sintered with each other. Defects on the side face of the scan vectors can be seen in the left view which look similar to defects in Fig. 5(a). In fact, defects found at the faces formed by the terminal points of the laser tracks and defects found on the side faces of the samples originate from the same process. Basically, the reason is lack of powder locally when placing two parallel laser tracks close to each other [25].

### 3.1.2. Scanning direction vertical to the front surface

Fig. 6(a) shows a micrograph of the front surface of sample T-3. As shown in Fig. 2, the scanning direction of sample T-3 is vertical to the front surface, and the front surface is composed of the initial points of the individual tracks. Fig. 6(b) shows the front surface of sample T-3 after sand blasting treatment. Pores distribute between tracks, and sand from sand blasting can also be seen on the surface. Comparing Fig. 6(a) and (b), many pores in Fig. 6(a) were covered by powder attached on the surface. Fig. 6(c) shows a micrograph of the back surface of sample T-3. As shown in Fig. 2, the back surface is made up by the terminal points of the individual tracks. During printing, the powder will shrink with laser scanning. Therefore, at the end of a track, there is less powder compared to the onset of the track. The lack of powder makes the back surface have larger pore structures. Fig. 6(d) shows a micrograph of the front surface of sample T-4. As shown in Fig. 2, the front surface is combined by initial and terminal points of individual tracks. Staircase structures formed by combining initial and terminal points can be seen in the micrograph. There are two reasons which may cause these staircase structures. First, like discussed before, lack of powder may cause the position of a terminal point to differ from that of the corresponding initial point. Second, the printing program also may be responsible for the position of an initial point not perfectly matching the terminal point position.

Fig. 7(a) shows the pressure drop during permeation tests on samples T-3 and T-4. The linear relation between pressure drop and superficial velocity confirms the applicability of Darcy's law. The permeability of the sample produced with an alternately opposite laser path is 1.72 times higher than for the sample with one direction laser path. Fig. 7(b) is the pore size distribution of samples T-3 and T-4 as derived from capillary flow porometry. The pore sizes of sample T-3 range from 2.6  $\mu\text{m}$  to 13.7  $\mu\text{m}$ , while sample T-4 shows a broader range from 4.2  $\mu\text{m}$

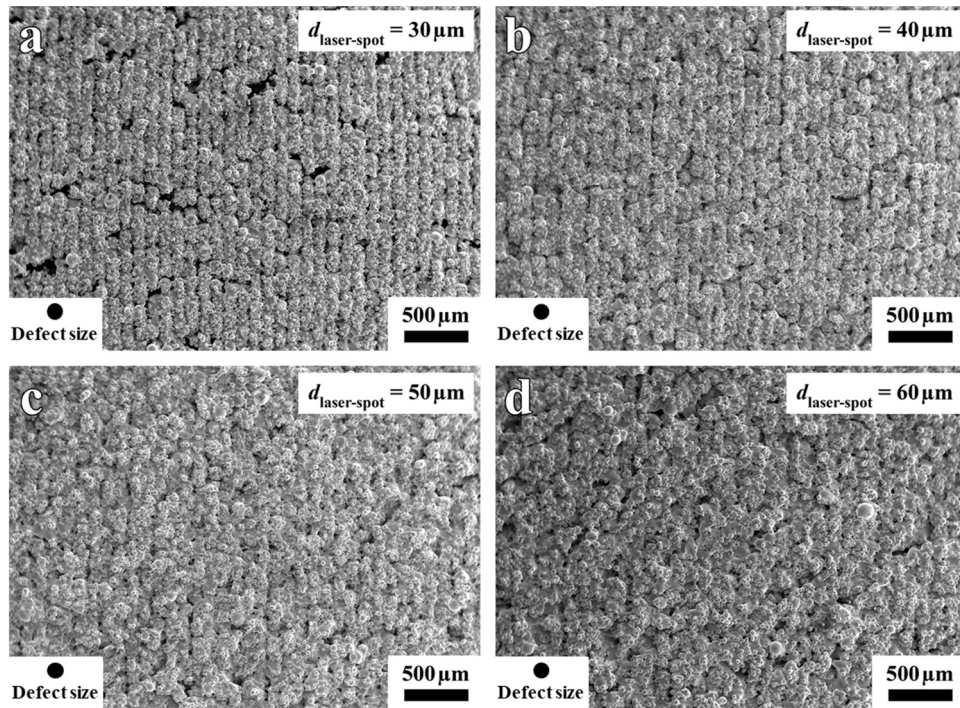


Fig. 8. SEM micrographs (magnification:  $\times 25$ ) of samples produced with different laser spot size.

to 75.2  $\mu\text{m}$ . Note that the method applied measures the smallest cross-sections of the through pores. Larger cross-sections of the same through pores are not detected. As discussed above, powder attached on the surface covers the pores on the surface of sample T-3. As shown in Fig. 6(d) the pores on the surface of sample T-4 cannot be fully covered due to the “staircase structure”. This could be one reason why sample T-4 shows a higher permeability and a wider pore size range.

Table 2 shows that different scanning paths didn't cause a drastic change in porosity. However, the roughness of sample T-4 is 1.52 times higher than that of sample T-3. As discussed, the reasons could be the powder attached on the surface and the staircase structure.

### 3.2. Influence of laser spot size on pore structure

Fig. 8 shows the surface structure of samples produced with different laser spot size in scan strategy A. The corresponding sample IDs are T-5, T-6, T-3, and T-7. Fig. 8(a) shows that there are many defects and gaps present on the front surface of sample T-5 (laser spot size: 30  $\mu\text{m}$ ). Fig. 8(b) shows that the powder attached on the surface covers the defects and gaps between the tracks on the front surface of sample T-6 (laser spot size: 40  $\mu\text{m}$ ). Fig. 8(c) and (d) show that powder attached on the surface is more obvious on the front surface of samples T-3 (laser spot size: 50  $\mu\text{m}$ ) and T-7 (laser spot size: 60  $\mu\text{m}$ ).

When the laser spot size is 30  $\mu\text{m}$ , laser energy is more concentrated. Powder consolidation causes a lot of defects on the front surface of the sample, and gaps between adjacent tracks are more obvious [25]. As the laser spot size increases, laser energy gets increasingly dispersed and so the powder attached on the surface causes defects to be covered and to disappear [26].

Fig. 9(a) shows the pressure drop during permeation tests on samples

obtained with different laser spot size. The linear relation between pressure drop and superficial velocity again confirms the applicability of Darcy's law. The permeability of sample T-5 (laser spot size: 30  $\mu\text{m}$ ) is 7.52 times higher than that of sample T-7 (laser spot size: 60  $\mu\text{m}$ ). Fig. 9(b) displays the pore size distribution of samples with different laser spot size. The pore size range of sample T-5 is from 7.2 to 120.3  $\mu\text{m}$  whereas the pore size of sample T-7 ranges from 2.8 to 17.1  $\mu\text{m}$ .

Fig. 9 illustrates that as the laser spot size increases, the permeability and pore size of the samples decrease. However, the data in Table 3 shows that the porosity of each sample is almost the same. One possible reason is powder attached on the surface covering the defects and impeding the liquid flow as discussed in the context of Fig. 8. The independence of pore size and permeability on porosity is a special feature of additively manufactured permeable materials.

When the laser spot size is 30  $\mu\text{m}$  or 40  $\mu\text{m}$ , the laser energy is more concentrated. There is less powder attached on the surface. Therefore, the roughness is increasing with increasing laser spot size. Usually roughness will also increase with larger hatch distance but the principle is different. A larger hatch distance will generate higher porosity which comes along with higher roughness. Increasing the laser spot size will cause more powder attached on the surface and this way increase the roughness. With different laser spot size, there should be more or less particle sintering on the surface.

### 3.3. Influence of hatch distance on pore structure

Fig. 10 shows micrographs of samples with different hatch distance. The corresponding sample IDs are T-3, T-8, T-9, T-10, T-11, T-12. With an increase of the hatch distance, the gaps between the tracks in Fig. 10(d)–(f) are more obvious than in Fig. 10(a)–(c). Powder attached on the

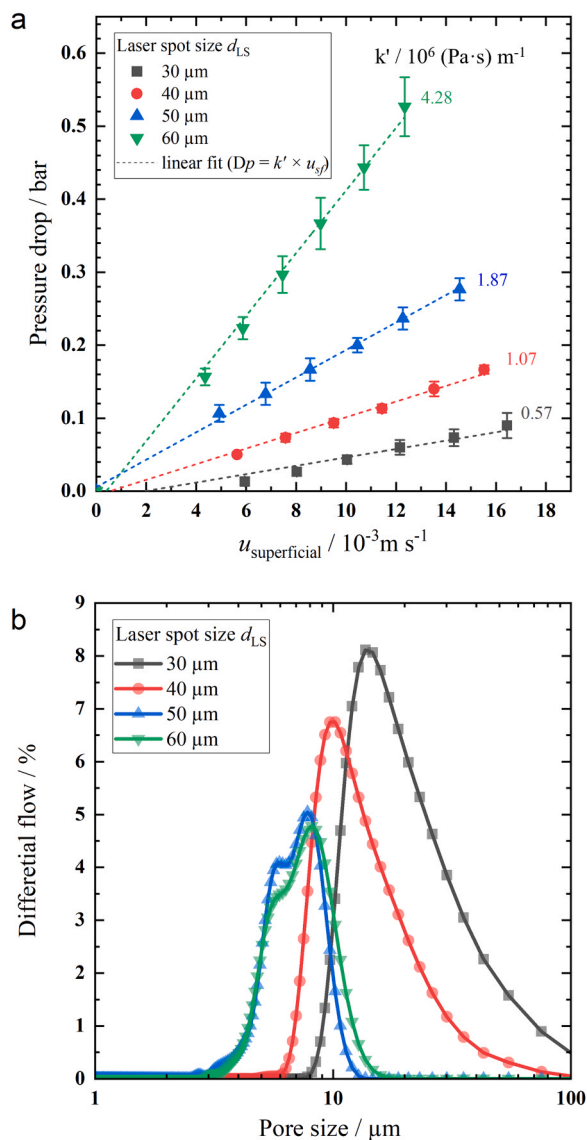


Fig. 9. (a) Permeation testing of samples with different laser spot size; (b) Pore size distribution of samples with different laser spot size.

surface is observed in all figures. However, due to the small gap width, powder attached on the surface is more effective in covering the gaps and generating smaller pores on the surface in case of Fig. 10(a)–(c). Whereas in Fig. 10(d)–(f), the effect of powder attached on the surface is not so obvious.

Table 3

Roughness, porosity, and permeability of samples with different laser spot size.

Print ID	T-5	T-6	T-3	T-7
Laser spot size	30 $\mu\text{m}$	40 $\mu\text{m}$	50 $\mu\text{m}$	60 $\mu\text{m}$
Roughness ( $\mu\text{m}$ )	19.66 $\pm$ 0.99	19.04 $\pm$ 0.41	20.37 $\pm$ 0.72	24.01 $\pm$ 0.62
Porosity	21%	15%	17%	16%
Permeability ( $\text{m}^2$ )	1.58 $\pm$ 0.11E-12	8.4 $\pm$ 0.23E-13	4.81 $\pm$ 0.14E-13	2.1 $\pm$ 0.07E-13

Fig. 11(a) shows the pressure drop during permeation testing on samples with different hatch distance. The linear relation between pressure drop and superficial velocity once more complies with Darcy's law. The permeability of T-11 (hatch distance: 0.14 mm) is 10.4 times higher than that of T-3 (hatch distance: 0.1 mm). Sample T-12 is not included because the pressure drop was too low to be measured accurately with the present setup. Fig. 11(b) shows the pore size distribution of samples with different laser spot size. The pore size range of T-11 is from 32.4  $\mu\text{m}$  to 84  $\mu\text{m}$ . The pore size range of T-3 is from 2.5  $\mu\text{m}$  to 13.7  $\mu\text{m}$ . With an increase of the hatch distance, permeability and pore size of the samples are gradually increased as shown in Fig. 11(a) and (b). Comparison to the analysis reported in Sections 3.2 and 3.3 yields that increasing the hatch distance is the most effective way to increase the permeability and the pore size. The factor by which the permeability is increased when increasing the hatch distance stepwise from 0.1 mm to 0.14 mm is: 1.23, 1.30, 2.63, 2.44. For a hatch distance higher than 0.13 mm, the rate of increase of the permeability accelerates significantly. According to the above analysis, an increase of the hatch distance weakens the effect of powder attached on the surface.

Table 4 shows the roughness, porosity, permeability and pore to throat size ratio of samples obtained with different hatch distance. From this table, it is clear that with increasing hatch distance roughness, porosity, and permeability all increase. The permeability and pore size distribution of samples with hatch distances of 0.1 mm, 0.11 mm, and 0.12 mm are closer to each other than for the other samples. As discussed, powder attached on the surface covering the defects on the surface could be the reason.

#### 4. Additively manufactured permeable-dense substrates for palladium composite membranes

The method established in this work for producing permeable-dense metallic parts was used to fabricate membrane supports for an ultra-compact integrated microchannel membrane reactor for steam methane reforming. Fig. 12. (a) shows the design of a laser-welded (*TruCell 3010, Trumpf*) membrane reformer module based on the stacking of microstructured plates made from the austenitic material Nicrofer® 3220H which was developed at the Institute for Micro Process Engineering over the last years [10,11,27]. The black area shows a Pd foil for hydrogen extraction from the reaction mixture sandwiched between two etched microsieves. The microsieves were coated with an 800 nm thick layer of  $\text{Y}_2\text{O}_3$ -stabilized  $\text{ZrO}_2$  (YSZ) by magnetron sputtering on the side in contact with the Pd foil to block the diffusion of metal atoms. For improved resistance against the differential pressure between the reforming section and the permeate section, the Pd foil welded between microsieve foils should be replaced by a composite Pd membrane coated on a mechanically stable permeable porous support. For this, the ferritic material Crofer® 22 APU was selected due to its lower thermal expansion coefficient, which is closer to that of Pd and the

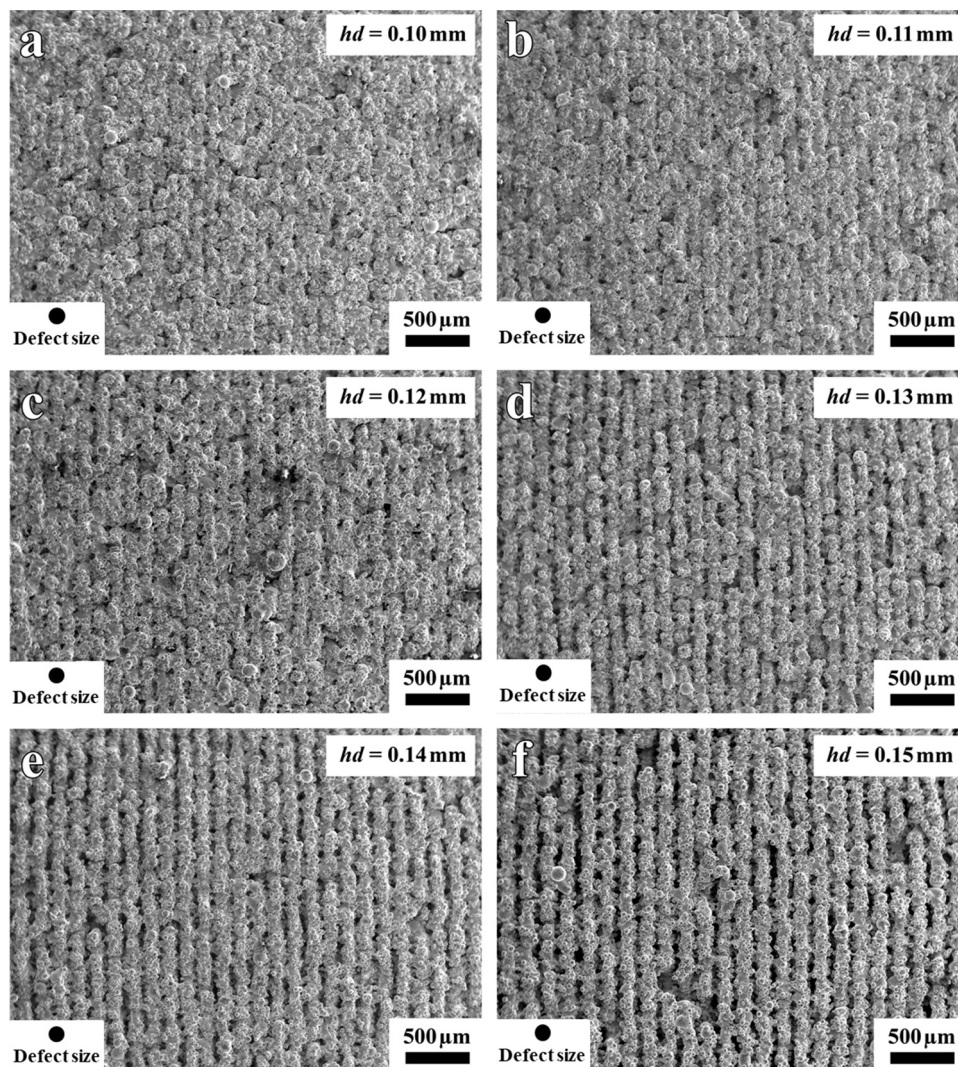


Fig. 10. SEM micrograph (magnification:  $\times 25$ ) of the front surface of samples with different hatch distance.

permeable ceramic diffusion barrier than that of Nicrofer® 3220H. The original concept was to laser-weld a permeable sheet made by tape casting into an impermeable frame and then dip-coat the permeable part by YSZ. However, substrates prepared this way are prone to the formation of defects in the YSZ coating in the area of the weld seam. Therefore, additively manufactured permeable-dense composites made from 316L stainless steel according to the method presented here were evaluated for coating with YSZ. Fig. 13(a) shows a test specimen made from Crofer® 22 APU the conventional way. Fig. 13(b) shows a specimen of the same type but made from 316L stainless steel by additive manufacturing. Fig. 13(c) provides a view of the conventionally made sample after YSZ coating. Cracks in the permeable area and defects in the weld seam area are visible which make successful coating with Pd difficult if not impossible. Fig. 13(d) shows the YSZ layer established with the same coating method on the additively manufactured

specimen. In this case, as there is no weld seam and the surface to be coated with YSZ does not show a marked change from the permeable to the impermeable region, neither cracks nor larger defects are visible in the YSZ coating. It is therefore expected that substrates prepared this way lead to improved Pd membrane quality.

Fig. 12(b) and (c) finally show a full size plate made from 316L stainless steel by additive manufacturing which shall replace the Pd foil sandwiched between the microsieves as well as the permeate channel plate shown in Fig. 12(a). This has been possible by combining a permeable front side (Fig. 12(b)) with an impermeable back side (Fig. 12(c)) and an impermeable frame and, in addition, establishing straight channels in between. To the best of our knowledge, this is the first time that a component like this has been made by laser beam powder bed fusion. For use in steam methane reforming, the final part must be produced from Crofer® 22 APU as the typical operating temperature is

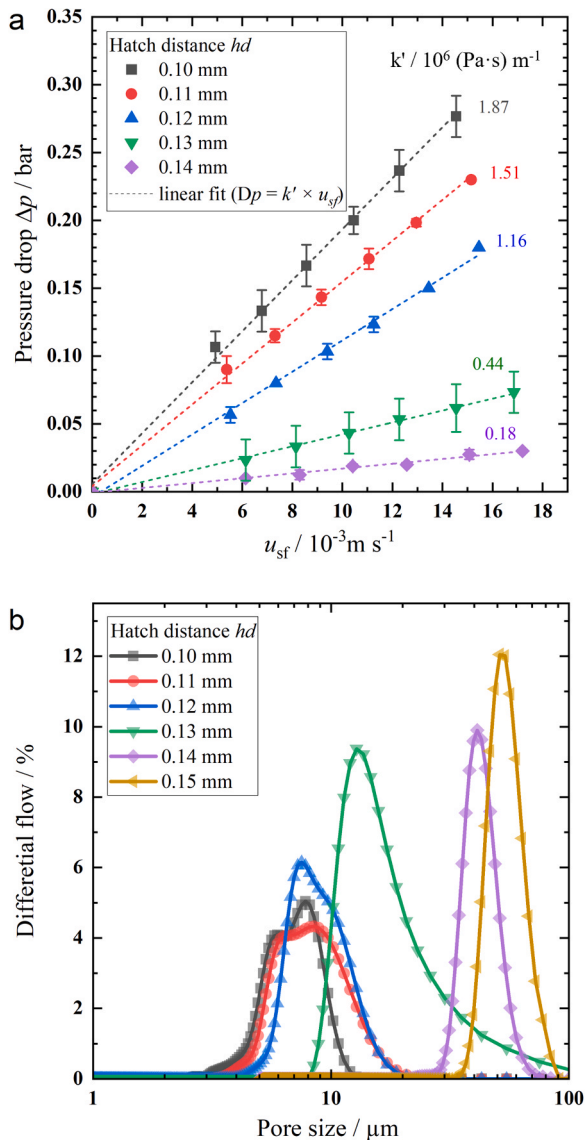


Fig. 11. (a) Permeation testing of samples with different hatch distance; (b) Pore size distribution of samples with different hatch distance.

550–600 °C. This is not yet available from the commercial powder suppliers for LB-PBF. To obtain comparable results like for 316L stainless steel will most likely require additional studies of the laser

Table 4  
Roughness, porosity, and permeability of samples with different hatch distance.

Print ID	T-3	T-9	T-10	T-11	T-12
Hatch distance	0.1 mm	0.11 mm	0.12 mm	0.13 mm	0.14 mm
Roughness ( $\mu\text{m}$ )	$20.37 \pm 0.72$	$20.7 \pm 1.44$	$24.94 \pm 1.14$	$27.7 \pm 1.25$	$32.74 \pm 0.56$
Porosity	17%	15%	19%	24%	26%
Permeability ( $\text{m}^2$ )	$4.81 \pm 0.14\text{E-13}$	$5.95 \pm 0.1\text{E-13}$	$7.74 \pm 0.14\text{E-13}$	$2.04 \pm 0.19\text{E-12}$	$4.99 \pm 0.26\text{E-12}$

parameters which are planned for the near future.

## 5. Conclusions

In this study, two kinds of pores in additively manufactured permeable materials are discussed. The pores within laser tracks are unstable and sensitive to the laser parameters. The pores between the tracks are easier to control, e.g., the direction of the pores can be controlled by altering the scanning direction of the laser. On this basis, the effect of different scanning strategies and parameters on the performance of the materials was systematically studied. The permeability of materials with similar porosity can be changed by using different scanning strategies or adjusting the laser spot. The key point of this method is the control of the powder attached on the surface. When this powder covers defects and pores on the samples' surface, the permeability and pore size will be decreased without changing the porosity. If the powder attached on the surface does not cover defects or pores, the permeability and pore size will increase while the porosity remains the same. By controlling the hatch distance, the porosity and pore size of the material can be changed in a wider range. To provide an illustrative example, the KIT logo was printed via permeable-dense structures in a flat plate. The logo shown in Fig. 14 was fabricated by controlling the scanning direction and the hatch distance. The triangle in the logo is made up by a large pore size material, while the other letters in the logo are formed by small pore size material. The remaining part of the logo is composed of dense material.

By accurately manipulating the parameters for permeable and dense structures, materials with various pore structure and dense structure can be printed in one go through LB-PBF. Based on this study, many interesting applications could be expected. Concrete systems under development at the Institute for Micro Process Engineering include engineered supports for palladium composite membranes like the one shown in Fig. 12(b) and (c) as key parts of an ultracompact modular membrane reactor system, internals for catalytic reactors with built-in product condensation and phase separation as well as structured parts in compact systems for distillation [27]. Others, for example, have developed self-catalytic reactors (SCR) with Fe, Co, Ni [28]. The semi spherical bulges in these structures showed better catalytic performance than traditional reaction tubes made by conventional manufacturing. From this perspective, permeable-dense composites could also be used for a new generation of SCRs.

## Author Contributions

The manuscript was written through contributions of all authors. All authors have given approval to the final version of the manuscript.

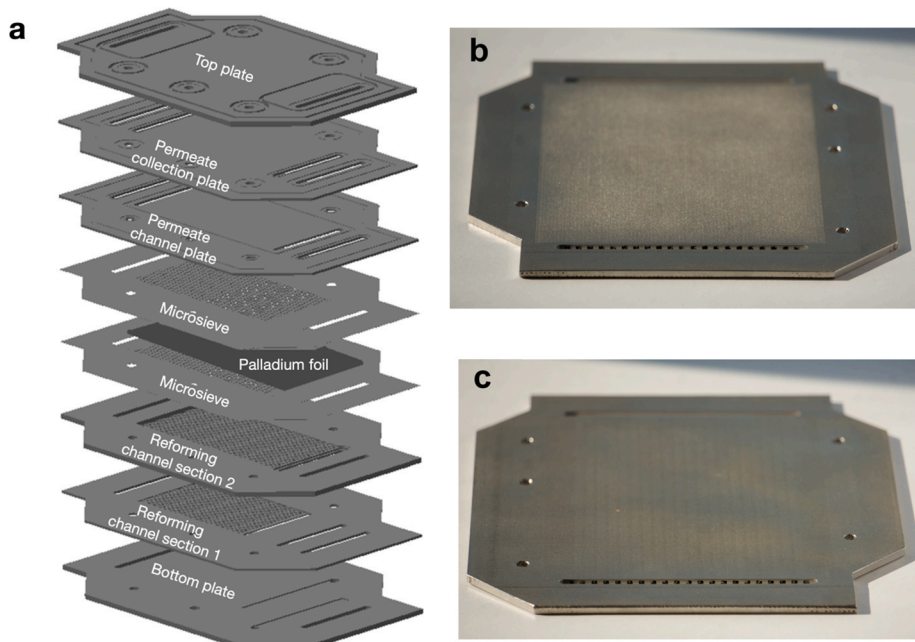


**Fig. 12.** (a) Stacked plate design of a compact integrated Pd membrane reactor module for steam reforming of methane with in situ hydrogen extraction from the reaction mixture [27]; (b) Additively manufactured permeable-dense substrate for coating with YSZ and Pd showing the rectangular permeable area on the front side. The substrate is made of 316L stainless steel and once coated with YSZ and Pd combines the Pd foil sandwiched between the microsieves as well as the permeate channel plate in one sheet; (c) Same substrate as in (b) but photographed from the back side showing a completely dense wall.

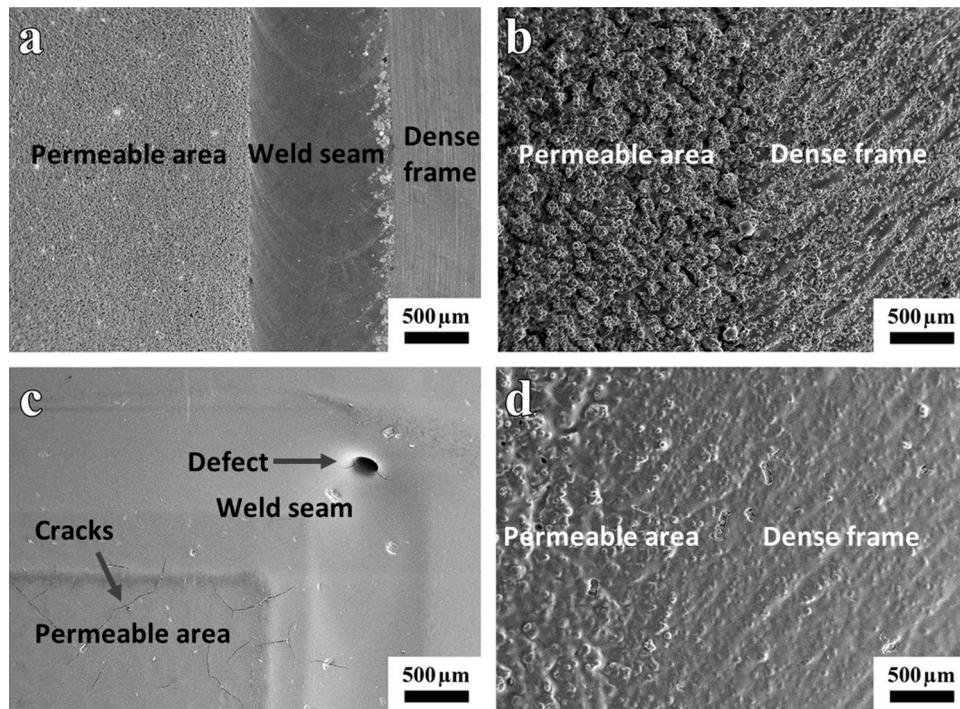


**Fig. 13.** (a) Conventional test module made from Crofer® 22 APU; (b) Additively manufactured test module made from 316L stainless steel; (c) Conventional test module after YSZ coating; (d) Additively manufactured test module after YSZ coating.

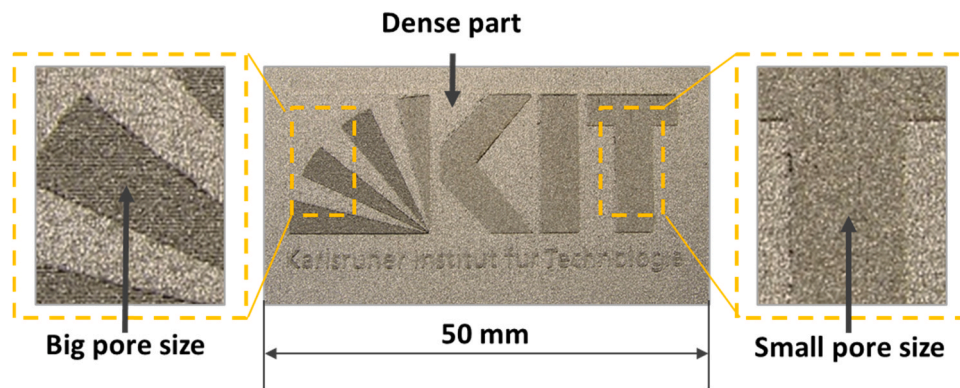


Fig. 14. Additively manufactured KIT logo.

### Declaration of Competing Interest

The authors declare the following financial interests/personal relationships which may be considered as potential competing interests: Dongxu Xie reports financial support was provided by China Scholarship Council.

### Acknowledgment

This research was supported by the China Scholarship Council, Beijing, P.R. China (fellowship to D. Xie, File No. 201706120030). The authors would like to thank Prof. A.I. Schäfer and her group from IAMT (KIT) for conducting the capillary flow porometry, Mr. Dahm and Mr. Walter from IAM-WBM (KIT) for tensile performance test, Mr. Hansjosten and Mr. Hofheinz from IMVT (KIT) for discussion regarding additive manufacturing, Ms. Yuan from IMVT (KIT) for permeability tests, Mr. Mahmoudizadeh from IMVT (KIT) for sand blasting and Mr. Wunsch from IMVT (KIT) for laser surface smoothing and Mr. Radel from MVM (KIT) for  $\mu$ -CT measurements.

### References

- [1] C.Y. Yap, C.K. Chua, Z.L. Dong, Z.H. Liu, D.Q. Zhang, L.E. Loh, S.L. Sing, Review of selective laser melting: materials and applications, *Appl. Phys. Rev.* 2 (2015), 041101, <https://doi.org/10.1063/1.4935926>.
- [2] D. Buchbinder, H. Schleifenbaum, S. Heidrich, W. Meiners, J. Bültmann, High power selective laser melting (HP SLM) of aluminum parts, *Phys. Procedia* 12 (2011) 271–278, <https://doi.org/10.1016/j.phpro.2011.03.035>.
- [3] H. Wang, X. Hu, Z. Ke, C.Z. Du, L. Zheng, C. Wang, Z. Yuan, Review: porous metal filters and membranes for oil-water separation, *Nanoscale Res. Lett.* 13 (2018) 284, <https://doi.org/10.1186/s11671-018-2693-0>.
- [4] X. Wang, S. Xu, S. Zhou, W. Xu, M. Leary, P. Choong, M. Qian, M. Brandt, Y.M. Xie, Topological design and additive manufacturing of porous metals for bone scaffolds and orthopaedic implants: a review, *Biomaterials* 83 (2016) 127–141, <https://doi.org/10.1016/j.biomaterials.2016.01.012>.
- [5] H. Stoffregen, J. Fischer, C. Siedelhofer, E. Abele, Selective laser melting of porous structures, in: *Solid Freeform Fabrication Proceedings*, 2011, pp. 680–695.
- [6] D. Xiao, Y. Yang, X. Su, J. Di Wang, Sun, An integrated approach of topology optimized design and selective laser melting process for titanium implants materials, *Biomed. Mater. Eng.* 23 (2013) 433–445, <https://doi.org/10.3233/BME-130765>.
- [7] E. Abele, H.A. Stoffregen, M. Kniepkamp, S. Lang, M. Hampe, Selective laser melting for manufacturing of thin-walled porous elements, *J. Mater. Process. Technol.* 215 (2015) 114–122, <https://doi.org/10.1016/j.jmatprotec.2014.07.017>.
- [8] J. van der Stok, O.P. van der Jagt, S. Amin Yavari, M.F.P. de Haas, J.H. Waarsing, H. Jahr, E.M.M. van Lieshout, P. Patka, J.A.N. Verhaar, A.A. Zadpoor, H. Weinans, Selective laser melting-produced porous titanium scaffolds regenerate bone in critical size cortical bone defects, *J. Orthop. Res.* 31 (2013) 792–799, <https://doi.org/10.1002/jor.22293>.
- [9] B. Dittmar, A. Behrens, N. Schödel, M. Rüttinger, T. Franco, G. Straczewski, R. Dittmeyer, Methane steam reforming operation and thermal stability of new porous metal supported tubular palladium composite membranes, *Int. J. Hydrogen Energy* 38 (2013) 8759–8771, <https://doi.org/10.1016/j.ijhydene.2013.05.030>.
- [10] T. Boeltken, D. Soysal, S. Lee, G. Straczewski, U. Gerhards, P. Peifer, J. Arnold, R. Dittmeyer, Perspectives of suspension plasma spraying of palladium nanoparticles for preparation of thin palladium composite membranes, *J. Membr. Sci.* 468 (2014) 233–241, <https://doi.org/10.1016/j.memsci.2014.06.003>.
- [11] P. Kant, Palladiumkompositmembranen durch Suspensionsplasmaspritzen auf planaren Substraten und deren Integration in kompakte Membranreaktoren, Master Thesis, Karlsruhe Institut für Technologie, 2017.
- [12] C. Klahn, F. Bechmann, S. Hofmann, M. Dinkel, C. Emmelmann, Laser additive manufacturing of gas permeable structures, *Phys. Procedia* 41 (2013) 873–880, <https://doi.org/10.1016/j.phpro.2013.03.161>.
- [13] A. Graichen, J. Larfeldt, D. Lörst, E. Munktel, E. Porous rotating machine component, combustor and manufacturing method, U.S. Patent 10,753,609[P], 25 August 2020.
- [14] S. Guddati, A.S.K. Kiran, M. Leavy, S. Ramakrishna, Recent advancements in additive manufacturing technologies for porous material applications, *Int. J. Adv. Manuf. Technol.* 105 (2019) 193–215, <https://doi.org/10.1007/s00170-019-04116-z>.
- [15] K. Cheng, W. Xiong, Y. Li, L. Hao, C. Yan, Z. Li, Z. Liu, Y. Wang, K. Essa, L. Lee, X. Gong, T. Peijs, In-situ deposition of three-dimensional graphene on selective laser melted copper scaffolds for high performance applications, *Compos. Part A: Appl. Sci. Manuf.* 135 (2020), 105904, <https://doi.org/10.1016/j.compositesa.2020.105904>.
- [16] L.F. Arenas, C. Ponce de León, F.C. Walsh, 3D-printed porous electrodes for advanced electrochemical flow reactors: a Ni/stainless steel electrode and its mass transport characteristics, *Electrochem. Commun.* 77 (2017) 133–137, <https://doi.org/10.1016/j.elecom.2017.03.009>.
- [17] D.I. Stoia, E. Linul, L. Marsavina, Influence of manufacturing parameters on mechanical properties of porous materials by selective laser sintering, *Materials* 12 (2019), <https://doi.org/10.3390/ma12060871>.
- [18] D.I. Stoia, L. Marşavina, E. Linul, Correlations between process parameters and outcome properties of laser-sintered polyamide, *Polymers* 11 (2019), <https://doi.org/10.3390/polym11111850>.
- [19] R. Li, J. Liu, Y. Shi, M. Du, Z. Xie, 316L Stainless steel with gradient porosity fabricated by selective laser melting, *J. Mater. Eng. Perform.* 19 (2010) 666–671, <https://doi.org/10.1007/s11665-009-9535-2>.
- [20] I. Yadroitsev, L. Thivillon, P. Bertrand, I. Smurov, Strategy of manufacturing components with designed internal structure by selective laser melting of metallic powder, *Appl. Surf. Sci.* 254 (2007) 980–983, <https://doi.org/10.1016/j.apsusc.2007.08.046>.
- [21] T. Furumoto, A. Koizumi, M.R. Alkahari, R. Anayama, A. Hosokawa, R. Tanaka, T. Ueda, Permeability and strength of a porous metal structure fabricated by additive manufacturing, *J. Mater. Process. Technol.* 219 (2015) 10–16, <https://doi.org/10.1016/j.jmatprotec.2014.11.043>.
- [22] J. Suryawanshi, K.G. Prashanth, U. Ramamurty, Mechanical behavior of selective laser melted 316L stainless steel, *Mater. Sci. Eng.: A* 696 (2017) 113–121, <https://doi.org/10.1016/j.msea.2017.04.058>.
- [23] J. Yu, X. Hu, Y. Huang, A modification of the bubble-point method to determine the pore-mouth size distribution of porous materials, *Sep. Purif. Technol.* 70 (2010) 314–319, <https://doi.org/10.1016/j.seppur.2009.10.013>.
- [24] I.G. Wenten, K. Khoiruddin, A.N. Hakim, N.F. Himma, The bubble gas transport method, in: N. Hilal, A.F. Ismail, T. Matsuura, D. Oatley-Radcliffe (Eds.), *Membrane Characterization*, Elsevier, Amsterdam, 2017, pp. 199–218.
- [25] I. Yadroitsev, A. Gusarov, I. Yadroitsava, I. Smurov, Single track formation in selective laser melting of metal powders, *J. Mater. Process. Technol.* 210 (2010) 1624–1631, <https://doi.org/10.1016/j.jmatprotec.2010.05.010>.
- [26] J.P. Kruth, L. Froyen, J. van Vaerenbergh, P. Mercelis, M. Rombouts, B. Lauwers, Selective laser melting of iron-based powder, *J. Mater. Process. Technol.* 149 (2004) 616–622, <https://doi.org/10.1016/j.jmatprotec.2003.11.051>.
- [27] A. Wunsch, P. Kant, M. Mohr, K. Haas-Santo, P. Pfeifer, R. Dittmeyer, Recent developments in compact membrane reactors with hydrogen separation, *Membranes* 8 (2018), <https://doi.org/10.3390/membranes8040107>.
- [28] Q. Wei, H. Li, G. Liu, Y. He, Y. Wang, Y.E. Tan, D. Wang, X. Peng, G. Yang, N. Tsubaki, Metal 3D printing technology for functional integration of catalytic system, *Nat. Commun.* 11 (2020) 4098, <https://doi.org/10.1038/s41467-020-17941-8>.